CHARPTER III

LITERATURE REVIEWS

This chapter is composed of several reports whose topics relate to this work. The viewpoints of this section include: the effects of zirconium content on structure and typical properties of $Ba(Zr_xTi_{1-x})O_3$ system, various techniques for improving BNT-properties, and the application of the combustion technique for synthesizing ferroelectric ceramics.

Barium zirconium titanate

The substitution of Zr^{4+} to Ti^{4+} to form $Ba(Zr_xTi_{1-x})O_3$ or BZT became interesting for more fundamental studies and also for some novel applications due to its excellent dielectric, tunability and promising piezoelectric and relaxor properties. The ferroelectric properties of BZT are largely dependent on the amount of Zr^{4+} substitution. At room temperature, this ceramics show normal ferroelectric behavior for $0 < x < 0.20$ and relaxor behavior when $x > 0.25$ [30].

As mentioned, $BaTiO_3$ exhibits a cubic phase at high temperature. By decreasing the temperature, the crystal structure is slightly distorted. The first phase transition occurs at ~120 °C and is called Curie temperature (T_c), in which the structure changes from a cubic to a tetragonal structure [25]. The next phase transition point, defined as T_{o-t} (~ 0 °C), is the phase transition-temperature from a tetragonal to an orthorhombic structure [25]. At -90 °C, the crystal structure is transformed from orthorhombic to rhombohedral. This point is defined as T_{r-o} [25]. Substitution of Zr^{4+} to Ti^{4+} induces T_{r-o} and T_{o-t} to increase, whereas T_c decreases [8]. When the Zr content is ~15 at.%, all the above three phase transition temperatures T_{o-t}, T_{r-o} and T_c merge near room temperature as reported by Dixit et al. [30]. The schematic diagrams of phase transition temperatures shifted and pinch phase transition are shown in Figure 17(a) and (b), respectively.

T GD
S16
P574f
2013

สำนักหอสมุด
i.63989 11
๓ - ต.ค. ๒๕๕๖

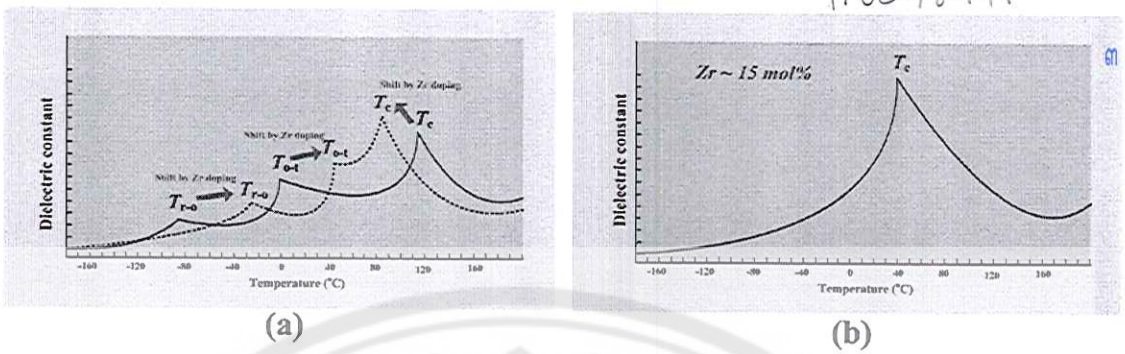

(a) (b)

Figure 17 Schematic diagram of how the Zr doped affects the phase transition temperatures of barium titanate

Effects of zirconium content on structure and typical properties of BZT ceramics

1. **Crystal structure**

There are different reports about how the crystal structure of $BaTiO_3$ is changed due to Zr substitution [5, 6, 7, 8]. Some groups reported the crystal structure of $BaTiO_3$ shows a tetragonal phase and substitution of Zr caused the tetragonality to increase. Chen, et al. [6] studied the crystal structure of $Ba(Zr_xTi_{1-x})O_3$ with $0.05 \leq x \leq 0.20$. The result demonstrated that BZT exhibited a tetragonal structure in all compositions. By increasing zirconium substitution, the lattice parameter a was increased while the lattice parameter c decreased. For $Ba(Zr_xTi_{1-x})O_3$ with $x = 0.2$, a c/a ratio of around 1.01 was observed as shown in Figure 18. Huang *et al.* [31] investigated the structure of $Ba(Zr_xTi_{1-x})O_3$ with x lower than 15 mol% by using XRD patterns. The results suggested that by increasing the zirconium content, the lattice parameters a and c were increased and the tetragonality approached 1 at 15 mol% zirconium substitution. Neirman, et al. [32] has also pointed out that as zirconium increased, both lattice parameters c and a were increased because the larger Zr^{4+} ionic radius (0.087 nm) is larger than that of Ti^{4+} (0.068 nm). However, the ratio of c/a decreased and when the zirconium content was higher than 10 mol%, the lattice constant increased in direct proportion to the increasing zirconium content.

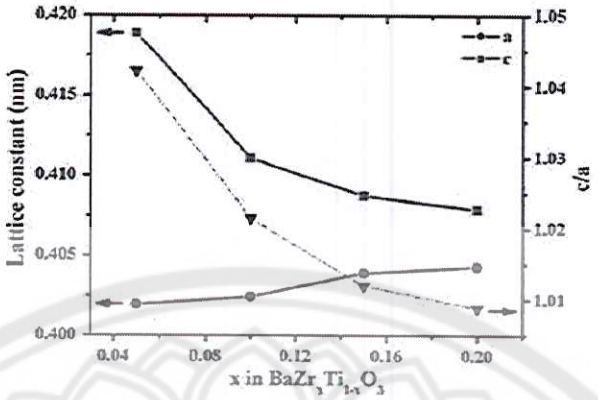

Figure 18 Dependences of the *a*- and *c*-axis lattice constants and *c/a* ratio (right hand side ordinate) on Zr/Ti ratio at room temperature [6]

Many researchers have reported the crystal structure of BZT from other viewpoints. Dixit, et al. [30] investigated the phase transition behavior of $Ba(Zr_xTi_{1-x})O_3$ with $0 \leq x \leq 0.4$. The report explained that the crystal structure of BZT depended upon the amount of Zr. BZT may have a tetragonal, orthorhombic, rhombohedral or cubic structure at room temperature. However, this report did not clearly explain the crystal structure of BZT for each composition. Kuang, et al. [8] studied the influence of Zr doped on properties of $Ba(Zr_xTi_{1-x})O_3$ with $0 \leq x \leq 0.12$. The report suggested that BZT exhibited a tetragonal phase at room temperature and that the crystal structure underwent a transformation from tetragonal to orthorhombic when zirconium content was increased. Binhayeeniyi, et al. [9] studied the crystal structure of $Ba(Zr_xTi_{1-x})O_3$ with $0 \leq x \leq 0.2$ using the Raman spectra and the XRD patterns. The report showed that is not possible to identify the crystalline phase of $Ba(Zr_xTi_{1-x})O_3$ with $0.00 \leq x \leq 0.02$ composition due to the close proximity of the diffraction angles. When the Zr content reached 10 mol%, the analysis results indicated that the crystal structure of BZT transformed from the orthorhombic to the rhombohedral phase and the structure was changed to a cubic phase when the zirconium content reached 20 mol%. The difference in the reports about the crystal structure of BZT*x* were summarized and are shown in Figure 19.

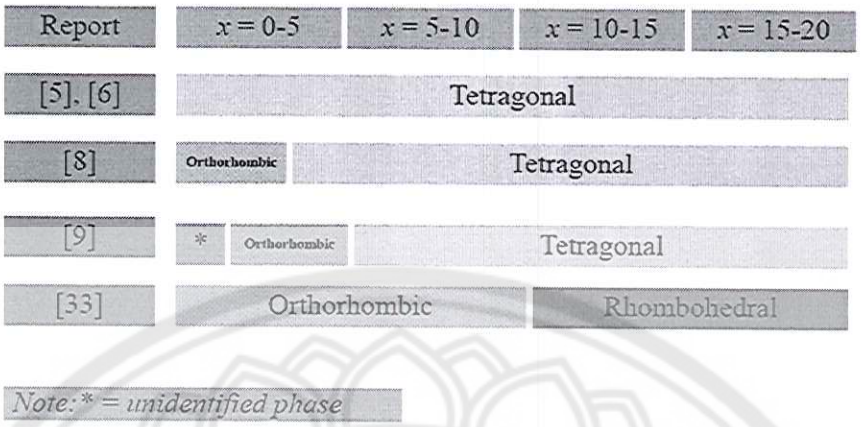

Figure 19 Phase identification of BZT ceramics with variation of mol% zirconium of *x* reported by several literatures

2. Dielectric constant

The substitution of Zr^{4+} to Ti^{4+} highly influenced the dielectric constant of $BaTiO_3$ [6, 8, 31, 34]. However, the effects of zirconium content on the dielectric properties of BZT show different characteristics. Chen, et al. [6] investigated the temperature dependence of the dielectric permittivity of BZT ceramics with various stoichiometric percentages of zirconium from 5 to 20 mol% (Figure 20). The results demonstrated that the value of maximum permittivity decreased as the zirconium content increased. Meanwhile, the permittivity of BZT ceramics with a higher zirconium content exhibited broad peaks. The broadness indicated the diffuse phase transition from a ferroelectric to a paraelectric phase. Moreover, the diffuse transition behavior was enhanced with increasing zirconium content, indicating a composition induced diffuse transition. Yu, et al. [34] investigated the dielectric properties of $Ba(Zr_xTi_{1-x})O_3$ with $0 \leq x \leq 0.3$. The study showed permittivity displays an irregular change with variations of Zr concentration, and shows a maximum of 46,000 at a Zr concentration of $x = 0.08$ in region I (Figure 21). This might be partially related to its grain size variation, which depends on both the processing and Zr concentrations. The increase and decrease of the maximum dielectric constant due to an increase of the zirconium content as reported by other groups is exhibited and summarized in Figure 22.

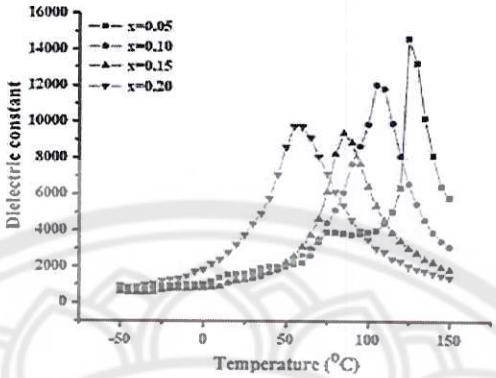

Figure 20 Temperature dependence of the relative permittivity of $Ba(Zr_xTi_{1-x})O_3$ ceramics at 1 kHz [6]

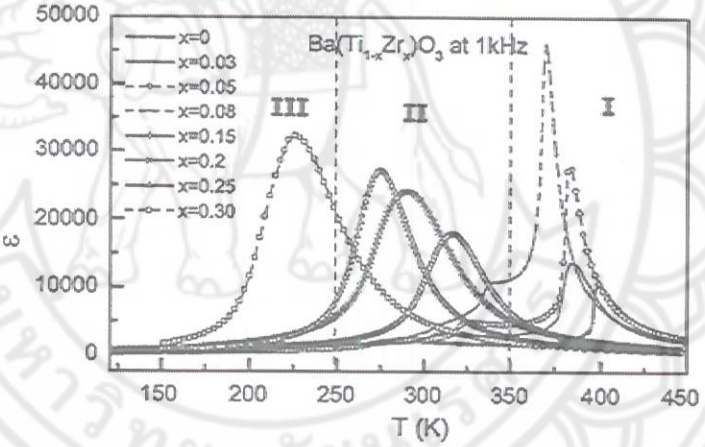

Figure 21 Temperature dependence of dielectric constant ε at 1 kHz for the $Ba(Zr_xTi_{1-x})O_3$ ceramics with x = 0, 0.03, 0.05, 0.08, 0.15, 0.2, 0.25 and 0.3 [34]

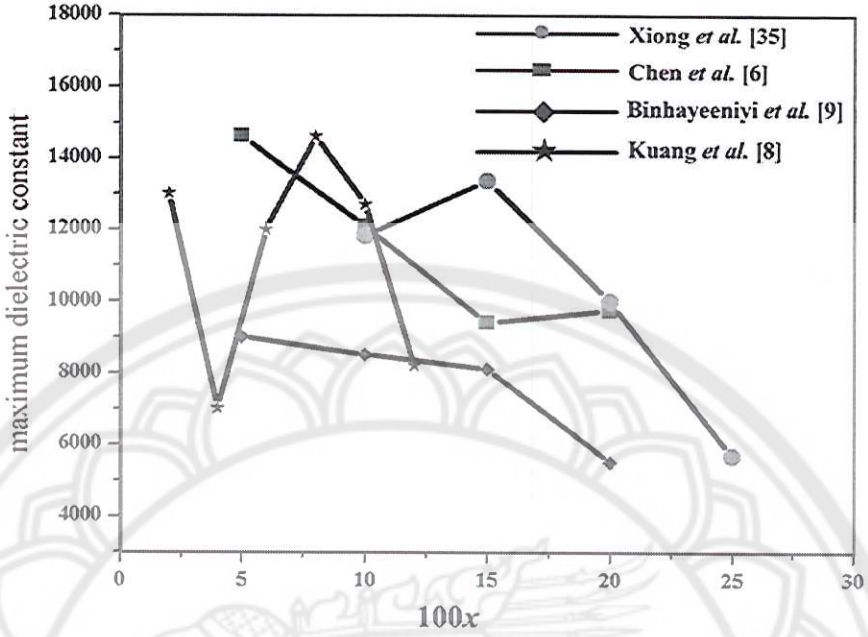

Figure 22 Variation of maximum dielectric constant of $Ba(Zr_xTi_{1-x})O_3$ from the literatures

3. Phase transition temperatures

The transition temperature of $BaTiO_3$ can be shifted when doped with isovalent ions substitution. Ba^{2+} can be replaced by isovalent ions with r_{12} radii between 130 and 160 pm (such as Pb^{2+}, Sr^{2+} and Ca^{2+}). Ti^{4+} can be replaced by isovalent ions with r_6 radii between 60 and 75 pm (such as Zr^{4+} and Sn^{4+}). For Ti^{4+} replaced by Zr^{4+}, they reduce T_c but raise the temperature of the other two transitions [25].

Nanakorn, et al. [10] studied the phase transition temperature of $Ba(Zr_x Ti_{1-x})O_3$ ceramics with $0.00 \leq x \leq 0.08$ from the temperature dependence of the dielectric curve as shown in Figure 23. They found that with increasing Zr content (0–5 mol %), the transition temperatures from tetragonal to orthorhombic structure (T_1) shifts toward higher temperatures. Transition temperatures from orthorhombic to rhombohedral (T_2) are clearly shown only at $x = 0.05$. At $x = 0.08$, the diffuse phase transition occurs resulting in an unclear phase transition temperature (T_1 and T_2). The transition temperatures and Curie temperatures of the BZT based compositions were recorded and are summarized in Table 1.

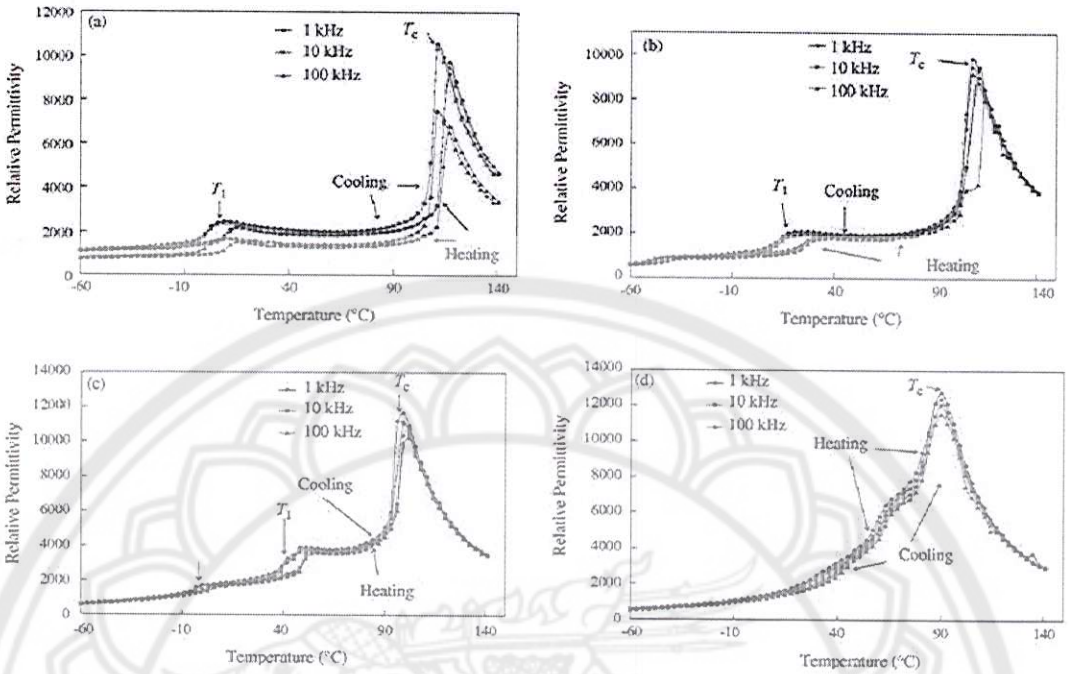

Figure 23 Temperature dependence of the relative permittivity for $Ba(Zr_xTi_{1-x})O_3$ ceramics with (a) $x = 0$ sintered at 1300 °C, (b) $x = 0.02$ sintered at 1350 °C, (c) $x = 0.05$ sintered at 1450 °C and (d) $x = 0.08$ sintered at 1400 °C at 1 kHz, 10 kHz and 100 kHz [10]

Table 1 The phase transition temperature (T_1, T_2 and T_c) of BZT ceramics [10]

$Ba(Zr_xTi_{1-x})O_3$	T_1 (°C)	T_2 (°C)	T_c (°C)
$x = 0.00$	6	-	117
$x = 0.02$	18	-	111
$x = 0.05$	42	0	102
$x = 0.08$	-	-	90

Kuang, et al. [8] plotted T_c (phase transition temperature from tetragonal to cubic structure), T_{o-t} (phase transition temperature from orthorhombic to tetragonal structure) and ε_m (maximum dielectric permittivity) as a function of zirconium content at 10 kHz for $Ba(Zr_xTi_{1-x})O_3$ ceramics with $0 < x < 0.12$ (Figure 24). The T_{o-t}

increased nonlinearly from 33 to 80 °C with increasing x from 0.02 to 0.10, respectively. Furthermore, the T_{o-t} peak decreased with increasing x. The phenomenon of decreasing T_c with increasing x can be explained in two ways. The first is because the radius of the Zr^{4+} is larger than that of the Ti^{4+} ion. The substitution of Zr^{4+} for Ti^{4+} will weaken the bonding force between the B-site ion and the oxygen ion of the ABO_3 perovskite structure. As the B–O bonds are weakened, the B-site ion can resume its position only when the tetragonal ferroelectric is at lower temperature, so the phase transition temperature is reduced. The second reason is because the weakening of the B–O bonds leads to a weaker distortion of the octahedron and the replacement also might induce a break of the cooperative vibration of the B–O chains. When this happens the *c/a* ratio is decreased. This break is responsible for the T_c of the BZT system, and thus a drop in Curie temperature was observed [8]. The values of T_c and T_{o-t} approached the same value when x is raised to ~0.12. The phase transition temperature from rhombehedral to orthorhombic (T_{r-o}), phase transition temperature from orthorhombic to tetragonal (T_{o-t}) and Curie temperature (T_c) dependence with zirconium content observed from literatures are listed in Table 2.

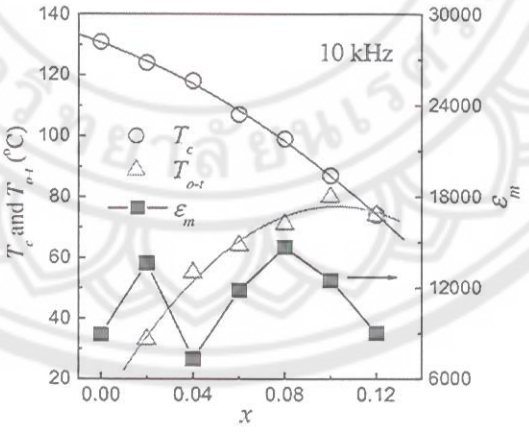

Figure 24 Phase transition temperature T_c, T_{o-t} and maximum dielectric permittivity ε_m as functions of zirconium content x at 10 kHz for $Ba(Zr_xTi_{1-x})O_3$ ceramics [8]

Table 2 $T_{r\text{-}o}$, $T_{o\text{-}t}$ and T_c as a function of zirconium content reported by literatures

Report	Composition of 100x of $Ba(Zr_xTi_{1-x})O_3$	$T_{r\text{-}o}$ (°C)	$T_{o\text{-}t}$ (°C)	T_c (°C)
Chen, et al.[6]	5			102
	10			89
	15			74
	20			55
Xiong, et al.[35]	10			90
	15			70
	20			40
	25			0
Kuang, et al.[8]	2		30	125
	4		55	118
	6		65	109
	8		70	100
	10		81	901
	12		75	75
Yu, et al.[34]	3	-33	27	107
	5	-13	47	102
	8	37	57	92
	15	-	-	37
	20	-	-	17
	25	-	-	-3
	30	-	-	-53

4. Ferroelectric polarization

The effects of zirconium content on the ferroelectric properties of BZT were investigated by Chen, et al. [6]. The results of well-behaved hysteresis loops of $Ba(Zr_xTi_{1-x})O_3$ with $x = 0.05$, 0.10, 0.15 and 0.20 are shown in Figure 25. It was found that the *P-E* hysteresis loop showed slimmer characteristics when the zirconium content increased.

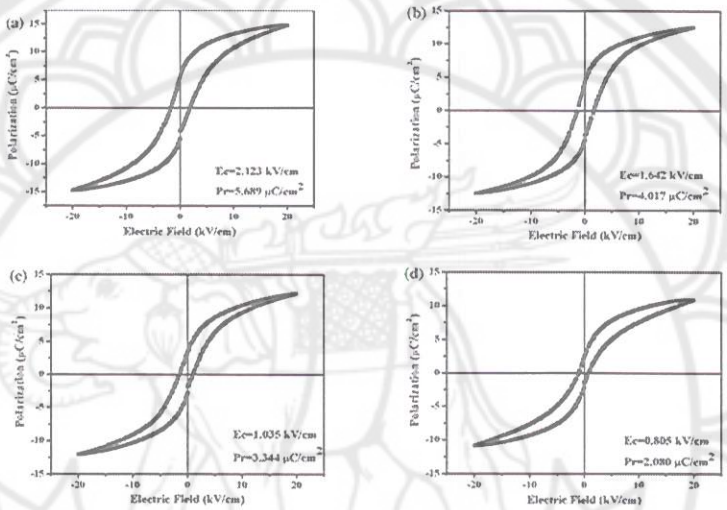

Figure 25 *P-E* Hysteresis loops of $Ba(Zr_xTi_{1-x})O_3$ ceramics at room temperature and 1 kHz with (a) $x = 0.05$, (b) $x = 0.10$, (c) $x = 0.15$, and (d) $x = 0.20$ [6]

Figure 26 shows the plot of the coercive electric field (E_c) and the remanent polarization (P_r) versus the stoichiometric percentage of zirconium. Both E_c and P_r decreased as zirconium content increased. Variation in remanent polarization in BZT ceramics can be explaine by the difference of radius in Zr^{4+} and Ti^{4+}. The decrease in E_c values with increasing zirconium content could be attributed to the increase in grain size as a result of the same sintering temperature. It is well known that a reversal polarization process in the ferroelectric domain is much easier inside a large grain than in a small grain.

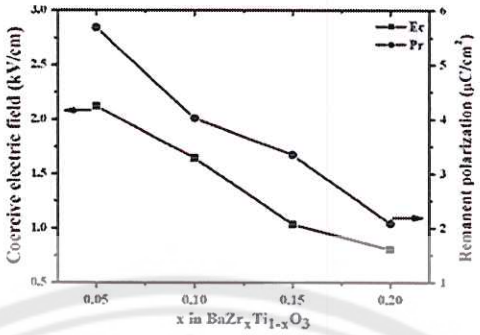

Figure 26 The E_c and P_r dependences of Zr/Ti ratio in $Ba(Zr_xTi_{1-x})O_3$ ceramics [6]

Nanakorn, et al. [10] investigated the effect of zirconium content and temperature on the *P-E* hysteresis loop of $Ba(Zr_xTi_{1-x})O_3$ ceramics with $0.00 \leq x \leq 0.08$. The report demonstrated that the loop altitude of the *P–E* hysteresis loops decreased with an increase in temperature when the temperature was raised and approached the Curie point (Figure 27). The variable of saturated polarization, remanent polarization and coercive field due to changing in zirconium content were listed in Table 3.

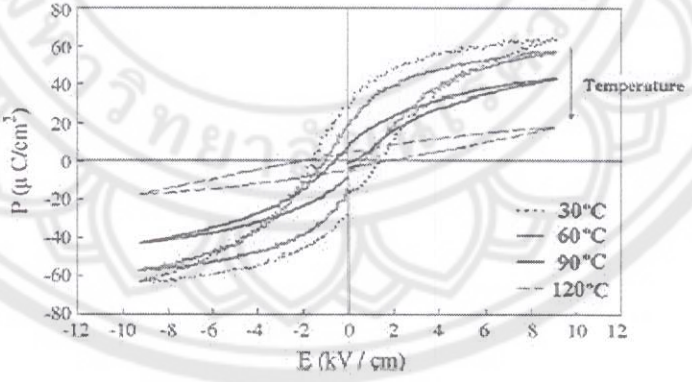

Figure 27 *P-E* hysteresis loop at the temperatures ranging from 30 °C to 120 °C of $BaZr_xTi_{1-x}O_3$ with $x = 0.08$ sintered at 1400 °C [10]

Table 3 The saturated polarization (P_s), remanent polarization (P_r), and coercive field (E_c) of BZT ceramics at 30 °C[10]

$Ba(Zr_xTi_{1-x})O_3$	P_s (μC/cm^2)	P_r (μC/cm^2)	E_c (kV/cm)
$x = 0.00$	35.862	4.424	0.696
$x = 0.02$	12.324	2.143	0.912
$x = 0.05$	57.920	25.033	1.048
$x = 0.08$	63.320	29.451	1.344

Bismuth sodium titanate ($Bi_{0.5}Na_{0.5}TiO_3$, BNT)

Bismuth sodium titanate ($Bi_{0.5}Na_{0.5}TiO_3$, BNT) was discovered by Smolensky, et al. in 1960 [36]. In pure BNT, half of all A-site positions are placed by bismuth (3^+) ions and the other half with sodium (1^+) ions. The B-site positions are placed by titanium (4^+) ions. Even though bismuth and sodium have very different charges, there is only a short range ordering of the A-site ions [38-40].

Pure BNT is a rhombohedral ferroelectric at room temperature. The rhombohedral-tetragonal phase transition temperature and Curie temperature are 300 and 540 °C, respectively [37]. The curves of permittivity versus temperature of BNT display a very interesting hump anomaly around 185 °C. This temperature is called the depolarization temperature (T_d), which corresponds to the transition from a ferroelectric to an anti-ferroelectric state. The maximum permittivity occurs around 340 °C, which is defined as T_m [37]. However, the phase transition behaviors at T_d and T_m are complicated and are not yet fully understood [37, 41].

BNT is one of the most important lead-free piezoelectric materials with a perovskite structure because of its high ferroelectricity ($P_r = 38$ μC/cm^2) [36]. However, pure BNT piezoelectric ceramics are difficult to pole because of their relatively large coercive field (E_c = 73 kV/cm) and high electrical conductivity. It for this reason that ways to improve the production of pure BNT have been extensively studied.

Several techniques for improvement of BNT properties

1. Cation substituted BNT perovskite lattices

Yang, et al. [42] mentioned BKT doped to BNT for 16-20 mol% induce the morphotopic phase boundary (MPB) between rhombohedral–tetragonal, which enhanced the electrical properties of BNT. Thus, this group was investigated to discover the effects of $Bi_{0.5}K_{0.5}TiO_3$ (BKT) content on the phase structure, microstructure, dielectric and piezoelectric properties of BNT-xBKT ceramics with $0.1 \leq x \leq 0.2$. The samples were prepared via the solid-state reaction method, which were calcined and sintered at 850 °C and 1150-1200 °C, respectively. The crystal structure was studied using XRD pattern as shown in Figure 28.

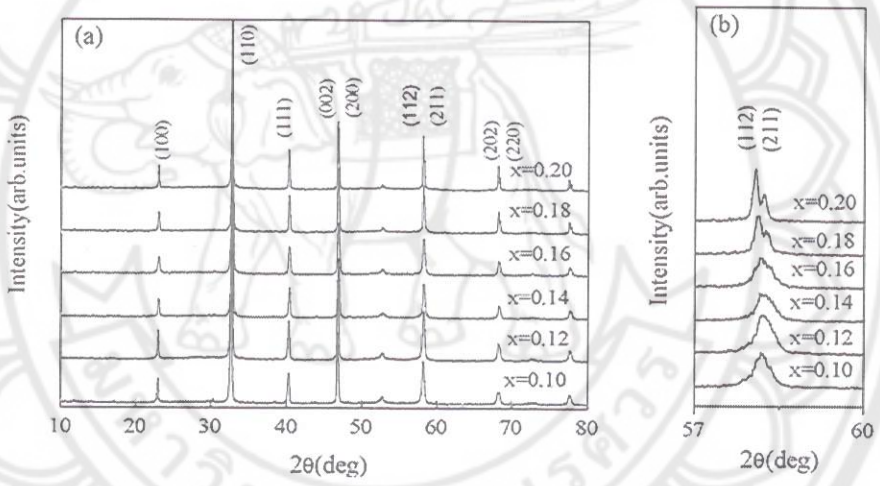

Figure 28 XRD patterns of BNT-xBKT powders [42]

From the XRD results, it can be clearly seen that the single peak of (211) at 2θ of 57° - 60° can be detected when $x < 0.16$. This suggests that the samples exhibit a rhombohedral structure. When $x = 0.16$, the diffraction peak begins to split. The (211) peak splits out to (211), (112), which indicates that the crystal was transformed to a tetragonal phase when $x = 0.18$ and 0.20. It can be concluded that the MPB is located at $0.16 \leq x \leq 0.20$. The results of the piezoelectric constant (d_{33}), electromechanical coupling factor (K_p), dielectric constant at room temperature (ε_r) and tanδ as a function of BKT content are shown in Figure 29. The results suggest that the electrical properties of BNT-xBKT ceramics tended to enhance by the increasing of x. The

maximums of d_{33} and K_p were obtained at $x = 0.18$ with the values of 144 pC/N and 0.29, respectively. This is because this composition is located near the MPB region.

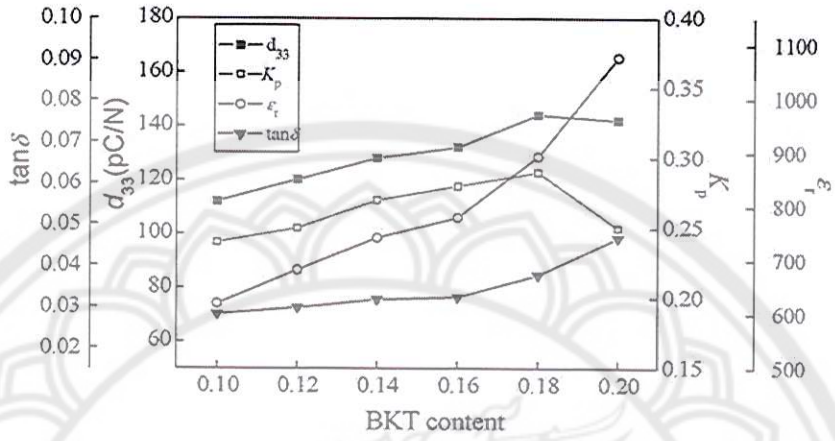

Figure 29 The piezoelectric constant d_{33}, electromechanical coupling factor K_p, dielectric constant at room temperature ε_r and tanδ as a function of BKT content [42]

Figure 30 shows the temperature dependence of ε_r and tanδ of BNT-xBKT ceramics measured at 1 kHz. There are two abnormal dielectric peaks in all samples with different compositions. The appearance of the first peak at T_t is caused when the phase is transformed from rhombohedral ferroelectric to tetragonal anti-ferroelectric. The appearance of the second peak at T_c can be explained by the transition from a tetragonal anti-ferroelectric to cubic paraelectric phase. It can be observed that the T_t shifts to lower temperature regions and the T_c shifts to higher temperature regions with increasing BKT content.

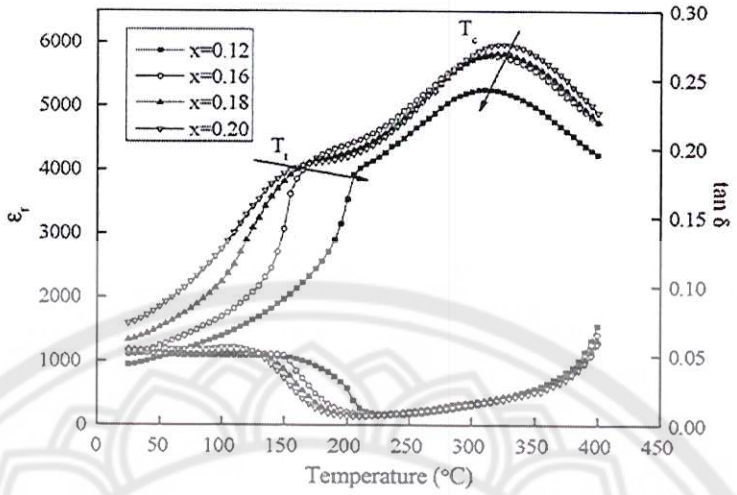

Figure 30 The temperature dependence of ε_r and tanδ of BNT-xBKT ceramics with different compositions [42]

The other some cation substituted to the A-site of BNT ceramics to improve BNT properties was the Li^{1+} ion. Lu, et al. [12] investigated the effects of Li and K being substituted in a BNT solid solution and recorded the effects on the crystal structure, dielectric properties and piezoelectric properties. The XRD patterns of the Li and K substituted BNT samples in the 2θ range of 20–70° and 38–50° are shown in Figure 31.

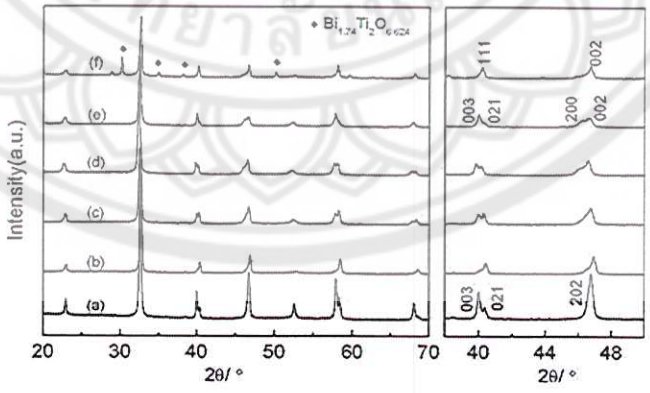

Figure 31 XRD patterns of Li and K substituted BNT ceramics; (a) BNT, (b) BNLT10, (c) BNKT10, (d) BNKT16, (e) BNKLT16-10 and (f) BNKLT16-35, in the 2θ range of 20–70° and 38–50°[12]

Generally, the symmetry of BNT at room temperature is a rhombohedral structure. This can be characterized by the splitting of (003)/(021) peaks at around 2θ of 40° and a single peak of (202) at around 2θ of 46.5°. $Bi_{0.5}K_{0.5}TiO_3$ is a perovskite type structure with tetragonal symmetry at room temperature which is characterized by the splitting of the (002)/(200) diffraction peaks at 2θ of 46.5°. The study results indicated that BNT, BNLT10 and BNKT10 have the same structure with a rhombohedral symmetry. The BNKT16 and BNKLT16-10 show the coexistence phases of a rhombohedral-tetragonal structure. With a further increase of Li content, the BNKLT16-35 shows a cubic structure and is accompanied with a secondary phase of $Bi_{1.74}Ti_2O_{6.624}$.

Figure 32 shows the temperature dependences of permittivity for Li and/or K substituted BNT ceramics at a frequency of 10 kHz. The permittivity of K doped BNT (BNKT16) ceramics is larger than that of BNT in the range of measurement temperature, especially the maximum permittivity. For Li doped BNT (BNLT10) ceramics, the permittivity is similar to pure BNT but is less than that of BNT when the temperature is higher than 200 °C. Moreover, the permittivity of K and Li doped BNT (BNKLT16-10) ceramics shows the mixing characteristics of K and Li doped BNT.

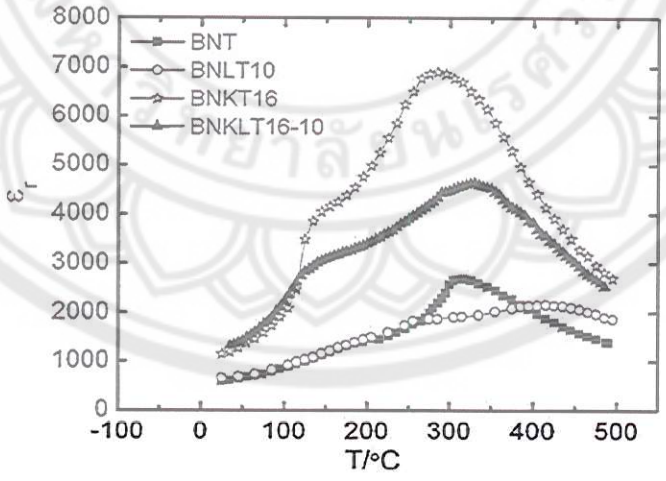

Figure 32 Temperature dependences of permittivity for Li and K substituted BNT ceramics at a frequency of 10 kHz [12]

The dielectric and piezoelectric properties of typical compositions of Li and K substituted BNT ceramics at room temperature are shown in Table 4. Li and/or K replacement for Na in BNT are improve the dielectric and piezoelectric properties, especially for the BNKLT1610 (near MPB) composition.

Table 4 Room-temperature dielectric and piezoelectric properties of BNT-based ceramics [12]

Compositions	BNT	BNLT10	BNKT10	BNKT16	BNKLT16-10
Piezoelectric constant d_{33} (pC/N)	78	95	105	138	160
Electromechanical coupling coefficient (k_p)	0.16	0.18	0.25	0.30	0.35
Dielectric permittivity ε_r at 25°C, 1 kHz	420	480	521	1020	1080
Dielectric loss $\tan\delta$ at 25°C, 1 kHz	0.03	0.036	0.023	0.029	0.038
Depolarization temperature, T_d (°C)	205	245	175	135	125
Curie temperature, T_C (°C)	315	365	285	295	335

2. Binary system of BNT-based

Chu, et al. [43] attempted to improve the electrical properties of BNT by investigating the MPB composition of the BNT-BT binary system. $(1-x)Na_{0.5}Bi_{0.5}TiO_3$–$xBaTiO_3$ with x = 0.02, 0.04, 0.06, 0.08 and 0.10 (abbreviated as NBBTx, x = 2, 4, 6, 8 and 10) were prepared via the conventional method. The X-ray diffraction patterns of the prepared samples are shown in Figure 33.

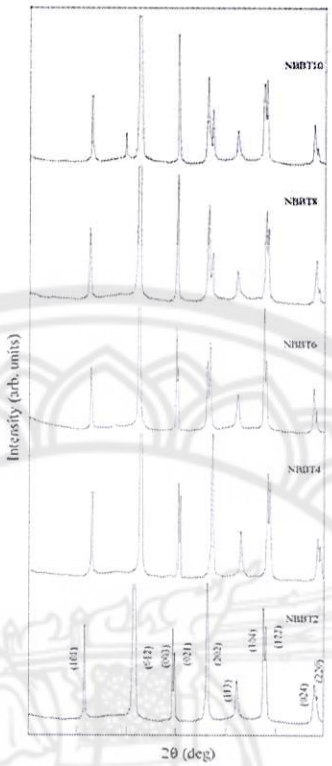

Figure 33 X-ray diffraction patterns of (1-*x*)$Na_{0.5}Bi_{0.5}TiO_3$–*x*$BaTiO_3$ ceramics[43]

At room temperature, the crystal structure of BNT is rhombohedral and that of BT is tetragonal. The X-ray diffraction revealed that NBBT2 and NBBT4 ceramics were in a rhombohedral phase. With increasing amount of $BaTiO_3$, the structures of NBBT8 and NBBT10 ceramics turned into a tetragonal symmetry characterized by (003) and (021) peaks combining into one peak and (202) peak splitting. The NBBT6 ceramics feature both rhombohedral and tetragonal symmetry. Therefore the MPB of (1-*x*)$Na_{0.5}Bi_{0.5}TiO_3$–*x*$BaTiO_3$ system is near $x = 0.06$.

The detailed electrical properties of NBBT*x* ceramics are shown in Table 5. The electrical properties of the (1-*x*)$Na_{0.5}Bi_{0.5}TiO_3$–*x*$BaTiO_3$ system, such as electromechanical coupling coefficient, piezoelectric constant and dielectric constant vary with the amount of $BaTiO_3$ and suggests that NBBT6 is the MPB composition.

Table 5 Electrical properties of (1-x)$Na_{0.5}Bi_{0.5}TiO_3$–$xBaTiO_3$ or NBBTx ceramics [43]

Property		Materials				
		NBBT2	NBBT4	NBBT6	NBBT8	NBBT10
Coupling factor	k_t	0.46	0.45	0.40	0.42	0.41
	k_p	0.20	0.21	0.29	0.13	0.14
Piezoelectric constant	d_{33}	78	87	122	112	94
Dielectric constant	ε^T_{33}	402	445	601	841	764
Frequency constant (Hz.m)	N_p	3190	3000	3000	2950	2980
	N_t	2680	2570	2522	2375	2418
Poisson ratio	σ	0.26	0.25	0.25	0.25	0.24
Dielectric loss	tgδ	0.0173	0.0207	0.0179	0.0204	0.0239
Maximum temperature of ε (°C)	T_m	265	230	225	250	180
Depolarization temperature (°C)	T_d	180	165	100	140	170
Remnant polarization(μC/cm^2)	P_r	37	-	40	36	22.5
Corecive field (V/mm)	E_c	4700	-	2880	3200	2880

Peng, et al. [44] studied the $(Bi_{0.5}Na_{0.5})TiO_3$ (BNT)-$Ba(Zr_{0.05}Ti_{0.95})O_3$ (BZT) binary system for (1-x)BNT–BZT100x with $x \leq 0.12$. The investigation focused on searching for MPB composition between BNT (rhombohedral) and BZT (tetragonal).

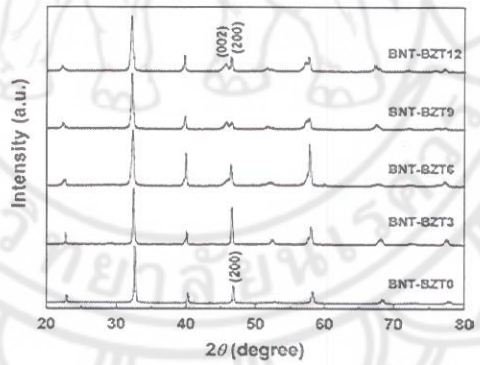

Figure 34 XRD patterns of BNT-BZT100x ceramics [44]

The X-ray diffraction patterns of BNT-BZT100x are shown in Figure 34. The splitting of (002)/(200) peaks from the single (200) peak showed that the crystal structure is transformed from rhombohedral to tetragonal due to an increase of BZT content. Moreover, the diffraction pattern of BNT-BZT9 suggested this has a MPB composition.

The $P-E$ hysteresis loops of the BNT-BZT ceramics a room temperature are shown in Figure 35. The results indicated that the BZT content highly influences the

ferroelectric properties of the system. The highest remanent polarization was exhibited in the BNT-BZT9 composition and it was near the MPB region

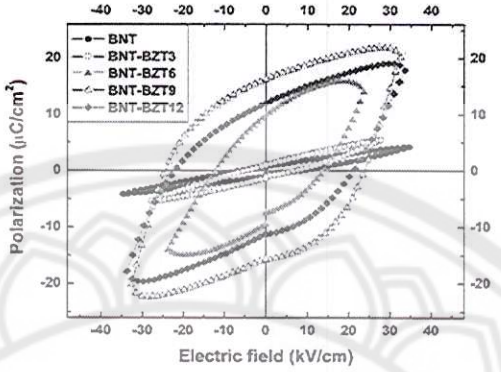

Figure 35 *P-E* loops of BNT–BZT100*x* ceramics with a maximum field of 40 kV/cm at room temperature [44]

The piezoelectric constant (d_{33}) and dielectric constant ($\varepsilon_{33}^{T}/\varepsilon_0$) of BNT–BZT ceramics altered with BZT fraction are listed in Table 6. The piezoelectric constant (d_{33}) increases with an increased BZT fraction up to 9 mol% and then decreases. The dielectric constant changes as a function of composition similarly to the piezoelectric constant, with a maximum value of 881.4 at 9 mol% BZT. The XRD pattern, piezoelectric and dielectric properties results support that BNT-BZT9 has a rhombohedral-tetragonal phase near the morphotropic phase boundary MPB.

Table 6 Piezoelectric, dielectric properties and density of BNT–BZT100*x* ceramics [44]

	d_{33} (pC/N)	T_c (°C)	ρ (g/cm^3)	$\varepsilon_{33}^{T}/\varepsilon_0$	$\tan\delta$ (%)
BNT	64	310	5.32	302.6	1.752
BNT-BZT3	79	236	5.76	345.6	1.765
BNT-BZT6	107	236	5.72	844.6	2.185
BNT-BZT9	147	244	5.82	881.4	2.636
BNT-BZT12	112	259	5.69	788.7	2.980

Investigation of the combustion technique for synthesizing ferroelectric materials

1. Typical organic compound selection as fuel

Hwang, et al. [20] investigated preparation of electronic ceramic oxide powders through the combustion technique. The organic compounds (e.g., glycine, urea, citric acid, alanine, or carbohydrazide) were mixed directly with the raw materials to synthesize $Ni_{0.5}Zn_{0.5}Fe_2O_4$ powders. Some of the properties of the five selected fuel types (alanine, glycine, carbohydrazine, urea, and citric acid) are listed in the Table 7.

Table 7 Some properties of organic compounds [20]

Properties	Organic component				
	Alanine	Glycine	Carbohydrazide	Urea	Citric acid
Structural formula	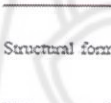	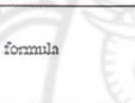	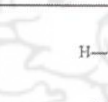		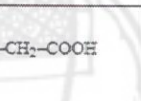
Molecular weight (g/mol)	80.1	90.1	75.1	60.1	192.1
Heat of combustion (kJ/g)	18.2	13.0	12.6	10.5	10.2
Decomposition temperature (°C)	314	262	153	135	175

The raw materials and organic fuel were mixed together in an equivalent stoichiometric ratio. The thermogravimetric analysis (TGA) of the precursor was investigated and is illustrated in Figure 36. Some organic fuels such as chabohydrazide and glycine showed that the slope of the weight loss–temperature curve was very steep. This indicated that the decomposition reaction of the fuel took place very rapidly. In case of citric acid, a distinct of three-stage weight loss was observed. When compared with other organic fuels, the slope of this curve is relatively flat which indicated that the reaction is more moderate. The analytical results obtained from synthesizing Ni–Zn ferrite products using various organic fuels is listed in Table 8. The results demonstrated that the combustion technique produces nanocrystalline and good chemically homogeneitic powders.

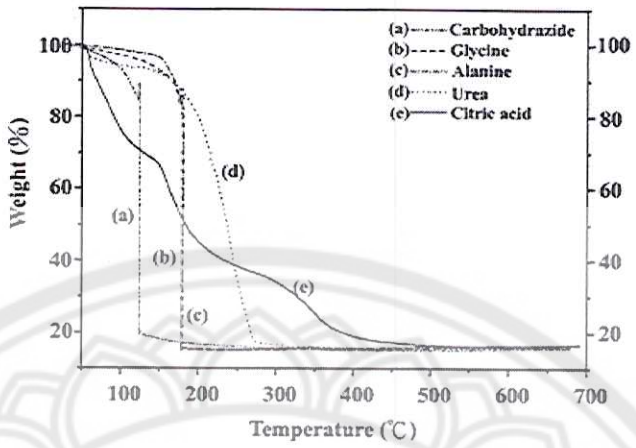

Figure 36 Typical TGA plots of the precursors prepared by using various fuels [20]

Table 8 Effects of various organic compounds and particular properties of Ni–Zn ferrite synthesized by the proposed combustion synthesis method [20]

Fuel	T_m[a] (°C)	Amount of gas produced (mole)	Crystallite size[b] (nm)	Surface area (m^2/g)	Carbon content (wt.%)	Ni^{2+}:Zn^{2+}:Fe^{3+} (molar ratio)	M_s[c] (Am^2/kg)
Alanine	1245	20.7	38.6	24.7	1.64	0.500:0.467:1.920	60.8
Glycine	1150	26.2	32.7	31.2	1.53	0.500:0.471:1.922	62.4
Carbohydrazide	1380	24.0	43.7	20.6	1.87	0.500:0.462:1.917	58.5
Urea	785	30.7	20.2	48.5	3.82	0.500:0.483:1.936	57.2
Citric acid	725	26.2	22.7	44.1	5.75	0.500:0.490:1.947	55.8

2. Decomposition reaction of the typical fuel (urea)

Eichelbaum, et al. [45] studied the decomposition reaction of urea using simultaneous thermogravimetric (TG), differential thermal analysis (DTA) and measured the gasses produce. The results are shown in Figure 37.

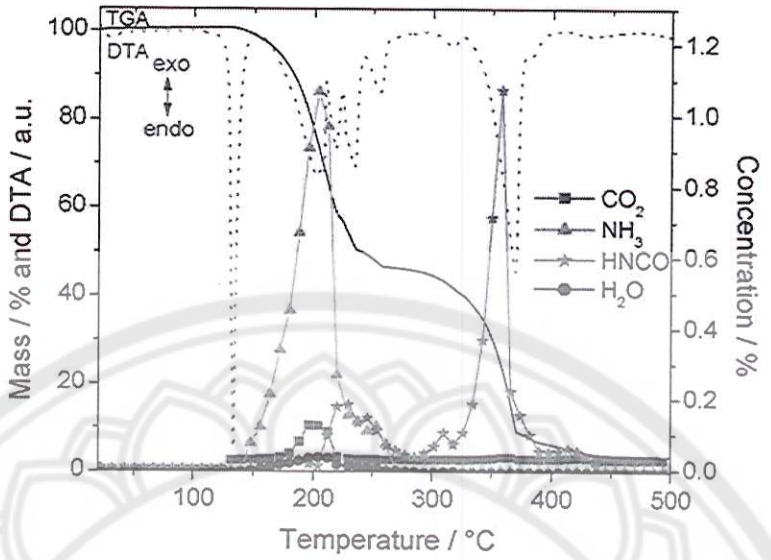

Figure 37 TGA, DTA graphs and quantitative results of the GC/MS evolved gas analysis [45]

The results revealed that the decomposition reactions of urea show multi-stages. Urea initially melted at 133 °C and then several decomposition reactions occurred between 150-250 °C. The main reaction consisted of the thermolysis of urea to ammonia (NH_3) and isocyanic acid (HNCO). However, only a minor amount of HNCO was detected between 210 and 270 °C. The weak production of CO_2 at 200 °C can be explained by the hydrolysis of HNCO with trace water in the original sample to NH_3 as shown in Figure 38(a). The other main reactions in this temperature range were the formation of ammelide. This started with the reaction between HNCO and urea to form biuret at a temperature higher than 150 °C and then the biuret reacted with HNCO to form ammelide as shown in Figure 38(b). Above 270 °C, cyanuric acid was formed from HNCO (Figure 38(c)). A large mass loss can be observed in the TGA spectrum (Figure 37) accompanied with a sharp endothermic peak at 370 °C and the production of large amounts of HNCO. This can be explained by the thermolysis of cyanuric acid, which decomposes above 300 °C (Figure 38(c)). At the same time, ammelide reacted with NH_3 and ammeline was formed at temperature higher than 270 °C (Figure 38(d)). Thereafter, the ammeline continuously decomposed to HNCO and cyanogens (CN_2) at high temperature as shown in Figure 38(e).

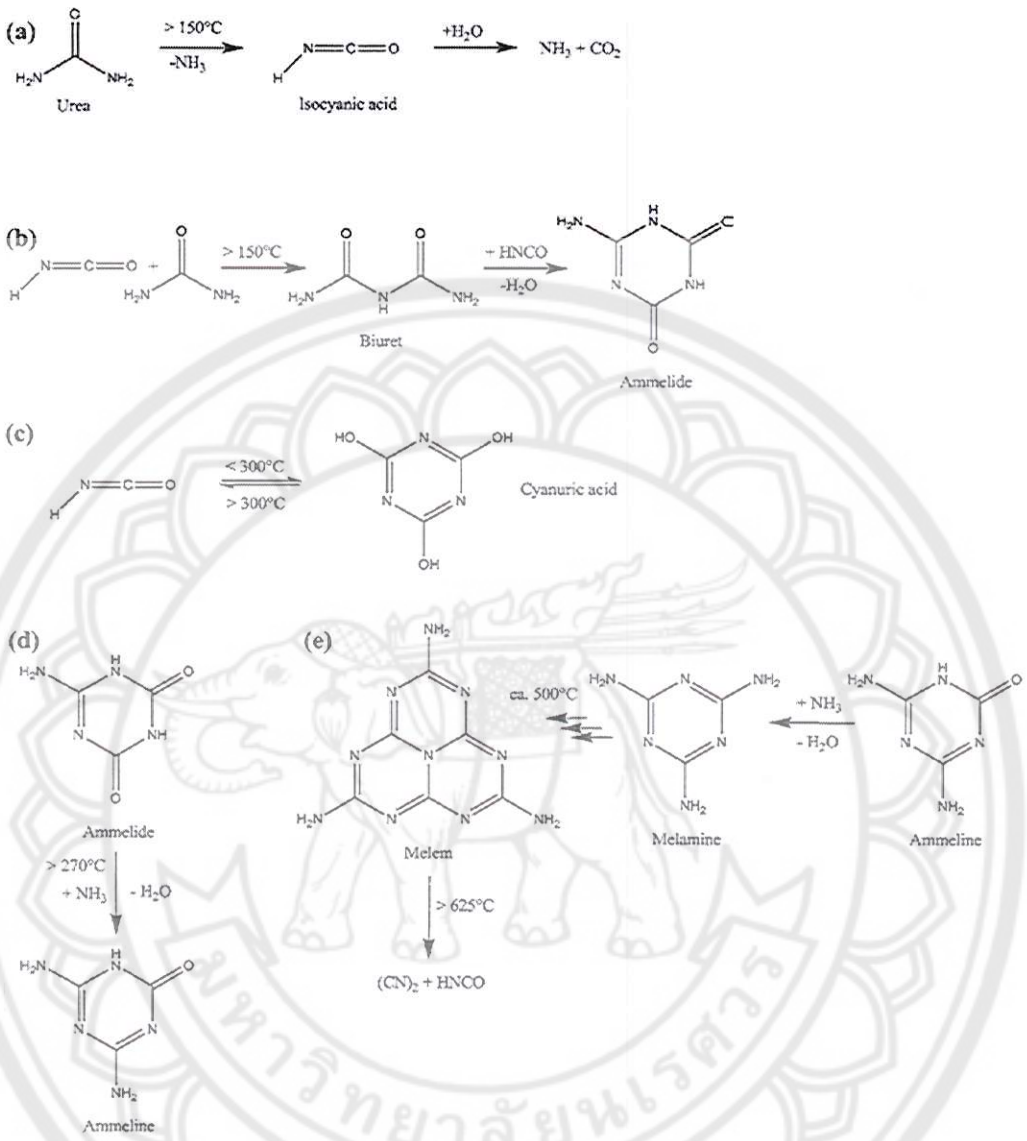

Figure 38 Schematic diagram of major decomposition reaction of urea [45]

3. Fuel content selection

The decomposition reactions of the organic compounds released high energy in multi-stages. Some research groups studied the synthesis of electroceramics with organic compound added, and expected the released energy from the decomposition reaction of fuel to be helpful in accelerating the chemical reaction of the raw materials [45-48]. Moreover, Hwang, et al. [20] suggested that the NH_3 released from the decomposition of organic compounds such as urea, glycine, alanine and citric acid could react with NO_x from the decomposed metal nitrate. The oxidation-reduction

reaction is shown in Eq.16. The energy released from this oxidation-reduction reaction accelerated the chemical reaction of raw materials.

$$4x\mathrm{NH_3} + 10\mathrm{NO}_x \rightarrow (5+2x)\mathrm{N_2} + 6x\mathrm{H_2O} + 2x\mathrm{O_2} \qquad \text{[Eq.16]}$$

There are two main energy releases during electroceramic synthesis in which the added raw materials consist of metal nitrate and organic compound. The first main energy is released from the decomposition reaction of fuel and the next one is released from the oxidation-reduction reaction between ammonia (decomposed from amine group of fuel) and NO_x (decomposed from metal nitrate of raw materials). This released energy helps to speed up the chemical reaction of the raw materials. However, it has been reported that an exothermic redox reaction (oxidation and reduction reaction taking place simultaneously) could be initiated only when the oxidizer and the fuel are mixed intimately in a fixed proportion. The basis of the combustion synthesis process is derived from the thermochemical concepts used in propellant chemistry [46, 47, 48, 49, 50, 51].

The ratio of the oxidizer and fuel for the redox mixture is calculated using the equivalence ratio (φ), defined as

$$\varphi = \frac{O}{F} \qquad \text{[Eq.17]}$$

Where (O) is the total oxidizing valence and (F) the total reducing valence of the elements present in the mixture [35]. According to propellant theory, the species M^{2+}, M^{3+}, M^{4+}, C and H are considered to be reducing with valencies of + 2, + 3,+ 4, + 4 and + 1 respectively. Oxygen is considered to be an oxidizing species with valence - 2 and nitrogen is considered to be valence neutral with a value of zero. Where the φ value is equal to unity (stoichiometric), the released energy reaches its maximum [46]. A mixture is fuel rich if $\varphi < 1$, fuel lean if $\varphi > 1$ [46].

Chavan, et al. [49] investigated the effects of oxidant-to-fuel ratio on the properties of Y_2O_3 synthesizing. The raw materials of $Y(NO_3)_3 \cdot 6H_2O$ and glycine (selected fuel) were mixed by the molar concentration in which the oxidant (yttrium nitrate) was kept constant at unity and the fuel concentration was varied. The elemental stoichiometric coefficient φ which is the ratio between the total valencies

of fuel (glycine; NH_2CH_2COOH) and that of the oxidizer (yttrium nitrate), can be calculated as shown below

$$\varphi = \frac{0_{(N)} + 2\times 1_{(H)} + 4_{(C)} + 2\times 1_{(H)} + 4_{(C)} - 2_{(O)} - 2_{(O)} + 1_{(H)}}{3_{(Y)} + 3\times 0_{(N)} + 9\times -2_{(O)}} \qquad \text{[Eq.18]}$$

In the present system, to satisfy this stoichiometric ratio the yttrium nitrate (oxidizing valency = 15−) to glycine (reducing valency = 9+) molar ratio was found to be 1:1.66. Previously the properties of powders had been studied by varying the molar ratios on either side of this ratio, i.e., fuel-lean compositions as 1:0.5, 1:1.0 and fuel rich i.e., 1:2.0, 1:2.5, 1:3.

Table 4 shows some properties of prepared powders with various oxidants to fuel ratio. The smallest crystallite size (8 nm) and the highest surface area (165 m^2/gm) were observed for the powder with a lean fuel condition (1:1.0). The powder with a stoichiometric composition had the largest crystallite size (30 nm) and the lowest surface area (57 m^2/gm). Thus the product with the best powder properties was the one from the lean fuel precursor, with an oxidant-to-fuel ratio of 1:1.0. These results could be attributed to two competing effects. The first one is the enthalpy of the reaction and the next is the subsequent flame temperatures associated with it and the number of moles of gaseous product evolved during combustion.

For the stoichiometric composition (1:1.66), which is a composition corresponding to the principle of propellant chemistry, the highest flame temperature observed (1440 °C) lead to large crystallites and a low surface area. Moreover, high temperature affects the prepared powders exhibited local partial sintering particle characteristics.

Increasing to a rich fuel composition (1:2.0, 1:2.5 and 1:3.0) decreased the flame temperature and there was no flame in the 1:3.0 composition. This was probably due to the lack of sufficient oxidant required for the complete combustion of the excess fuel. Moreover, increasing the fuel ratio caused the number of moles of gases released to also increase. These liberated gases dissipated the heat of combustion and limited the temperature rising, thus reducing the possibility of premature local partial sintering among the primary particles [49].

Table 9 Comparison of powder properties with different oxidant-to-fuel ratio [49]

Powders	O/F	Flame temperature (°C)	No. of moles of gases as per equation	Crystalline size (nm)	Surface area (m^2/g)	Sintered density (%)
a	1:0.5	No flame	11.88	12	44	-
b	1:1.0	No flame	13.00	8	165	97
c	1:1.66	1440	15.42	30	57	92
d	1:2.0	1200	17.50	25	147	94
e	1:2.5	1050	20.00	9	114	96
f	1:3.0	No flame	22.50	9	90	94